Imprints of primordial magnetic fields on intrinsic alignments of galaxies

Shohei Saga,[1,2,3,*] Maresuke Shiraishi,[4] Kazuyuki Akitsu,[5,6] and Teppei Okumura[7,8]

[1]*Institute for Advanced Research, Nagoya University, Furo-cho Chikusa-ku, Nagoya 464-8601, Japan*
[2]*Kobayashi-Maskawa Institute for the Origin of Particles and the Universe, Nagoya University, Chikusa-ku, Nagoya, 464-8602, Japan*
[3]*Sorbonne Université, CNRS, UMR7095, Institut d'Astrophysique de Paris, 98bis boulevard Arago, F-75014 Paris, France*
[4]*School of General and Management Studies, Suwa University of Science, Chino, Nagano 391-0292, Japan*
[5]*Theory Center, Institute of Particle and Nuclear Studies, KEK, Tsukuba, Ibaraki 305-0801, Japan*
[6]*School of Natural Sciences, Institute for Advanced Study, 1 Einstein Drive, Princeton, New Jersey 08540, USA*
[7]*Academia Sinica Institute of Astronomy and Astrophysics (ASIAA), No. 1, Section IV, Roosevelt Road, Taipei 10617, Taiwan*
[8]*Kavli Institute for the Physics and Mathematics of the Universe (WPI), UTIAS, The University of Tokyo, Kashiwa, Chiba 277-8583, Japan*

(Received 29 December 2023; accepted 25 January 2024; published 16 February 2024)

Primordial magnetic fields (PMFs) are one of the plausible candidates for the origin of the observed large-scale magnetic fields. While many proposals have been made for the generation mechanism of PMFs by earlier studies, it remains a subject of debate. In this paper, to obtain new insights into PMFs, we focus on the intrinsic alignments (IAs) of galaxies induced by the vector and tensor modes of the anisotropic stress of PMFs. The long-wavelength vector and tensor modes locally induce the tidal gravitational fields, leading to the characteristic distortions of the intrinsic ellipticity of galaxies. We investigate the shear E- and B-mode power spectra induced by the magnetic vector and tensor modes in the three-dimensional space, assuming the combination of galaxy imaging and galaxy redshift surveys. We find that the magnetic tensor mode dominates both the E- and B-mode spectra. In particular, the B-mode spectrum induced by the magnetic tensor mode plays a crucial role in constraining the amplitude of PMFs, even in the presence of the nonmagnetic scalar contribution to the B-mode spectrum arising from the one-loop effect. In future galaxy redshift surveys, such as the Euclid and Square Kilometre Array, the minimum detectable value reaches $\sim$30 nG, which can potentially get even smaller in proportion to the number of observed galaxies and reach $\sim\mathcal{O}(1\ \mathrm{nG})$. Measuring the IAs of galaxies would be a potential probe for PMFs in future galaxy surveys.

DOI: 10.1103/PhysRevD.109.043520

I. INTRODUCTION

Recent observations of high-energy TeV photons emitted from the distant blazars suggest the existence of large-scale magnetic fields, especially in intergalactic and void regions [1–6]. For instance, Ref. [1] has reported the lower bound 3×10^{-16} Gauss on the amplitude of intergalactic magnetic fields. Although the origin of such magnetic fields remains an open question, a number of theories have been proposed to explain them. An interesting scenario attracting much attention is the primordial origin, in which the primordial magnetic fields (PMFs) are generated in the early Universe, especially before the cosmic recombination epoch. Since PMFs are generated before the formation of stars or galaxies, we expect to observe PMFs as large-scale magnetic fields, not associated with astronomical objects (see, e.g., [7–9] for reviews).

There exists a variety of models for the generation of PMFs. In the presence of an interaction between electromagnetic fields and other fields that break the conformal invariance during inflation, the inflationary magnetogenesis takes place from the quantum fluctuations [10–22]. The coherent length of PMFs generated in this way can be beyond the horizon scales. During cosmological phase transitions, the bubble collisions and turbulence in the primordial plasma result in the generation of PMFs [23–25]. In the simple phase transition models, the coherent length of PMFs is generally shorter than the observed intergalactic magnetic field. However, recent works [26–29] have proposed a model that can generate

*shohei.saga@yukawa.kyoto-u.ac.jp

PMFs with sufficiently long coherent length. In postinflationary epochs, the Harrison mechanism [30] results in PMFs at $O(\mathrm{Mpc})$ scales in the primordial plasma. However, the amplitude is about 10^{-24} Gauss [31–34], which is smaller than the observed amplitude.

To distinguish magnetogenesis models through observations, many authors have investigated the impact of PMFs on cosmological observables, for instance, the effects of PMFs on the big bang nucleosynthesis [35–40], cosmic microwave background (CMB) anisotropies [41–51], CMB spectral distortions [52–54], and large-scale structure of the Universe [55–58]. While cosmological observations to date have provided some clues to the generation mechanism of PMFs, it is also worth exploring other ways to extract further information from future cosmological observations.

Motivated by the above, this paper focuses on the intrinsic alignments (IAs) of galaxy shapes as a novel probe for PMFs. In weak gravitational lensing observations, the IAs of galaxies have been recognized as a contaminant to the estimation of cosmological parameters [59–66] (also see Ref. [67] for a review). However, it has been shown that the IAs of galaxies offer a unique opportunity to constrain the cosmological parameter, growth of the large-scale structure, and the initial condition of the Universe, complementary to galaxy clustering [68–80]. More interestingly, using the galaxy samples in the Sloan Digital Sky Survey, Ref. [81] has measured the anisotropic signals of the IA due to redshift-space distortions and indeed used the signals to constrain the growth rate of the Universe.

How do PMFs leave their imprints on the IA? References [82–86] have shown that the long-wavelength vector and tensor metric perturbations induce the short-wavelength gravitational tidal fields, called the fossil effect. Such tidal fields are expected to affect the intrinsic shape of galaxies, leading to the IAs. The imprints of primordial gravitational waves (GWs) on the IAs have been analytically and numerically investigated [82–86]. Very recently, assuming the photometric surveys, Ref. [87] has investigated the impact of the primordial vorticity vector mode [42,88] and primordial GWs on the IAs. Since our primary interest lies in the IAs as a new probe of PMFs, this paper focuses on the vector and tensor modes induced by PMFs.

The anisotropic stress fluctuation of PMFs creates additional metric perturbations on standard nonmagnetic contributions [42,44–46]. The resultant metric perturbations source the IAs. As for the scalar mode, the magnetic contribution is not remarkable and hidden by the nonmagnetic one; thus, we shall not investigate it below. By elucidating the relation between the anisotropic stress of PMFs and the IAs, we derive the analytical expression of the E- and B-mode power spectra of the intrinsic ellipticity of galaxies induced by the vector and tensor modes of PMFs. Exploiting the derived analytical expression, we explore the potential to constrain the amplitude of PMFs in the Euclid and Square Kilometre Array (SKA) galaxy redshift survey as well as more idealistic cases.

This paper is organized as follows. In Sec. II, we briefly review the general properties of PMFs and present how the anisotropic stress of PMFs induces the vector and tensor modes. For comparison purposes, we also introduce the vorticity vector mode and primordial GWs. In Sec. III, based on Ref. [85], we show the analytical expression of the intrinsic ellipticity shape induced by the long-wavelength vector and tensor modes. We show the detailed derivations in Appendix A. In Sec. IV, we derive an analytical expression for the three-dimensional E- and B-mode power spectra, and see their typical behavior. Using the analytical expression of the E- and B-mode power spectra, we perform the Fisher matrix computation and derive the expected minimum detectable value of the amplitude of PMFs in future surveys in Sec. V. In our analysis, we take into account the nonmagnetic scalar mode contributions to the E- and B-mode power spectra, respectively arising from the leading-order and one-loop order effects. We present the way to compute the one-loop B-mode spectrum in Appendix B. We perform the same analysis for the vorticity vector mode and primordial GWs in Appendix C. Section VI is devoted to the summary of our findings. Throughout this paper, we apply the Einstein summation convention for repeated Greek indices and alphabets running from 0 to 3 and from 1 to 3, respectively. We work in units $c = \hbar = 1$.

II. VECTOR AND TENSOR MODES

We are interested in imprints of the vector and tensor modes induced by PMFs on cosmological observables. In this section, we briefly introduce the basic property of the initial power spectrum of PMFs and the vector and tensor modes induced by PMFs in Sec. II A. We also introduce other possible cosmological sources to generate the vector and tensor modes in Sec. II B for comparison purposes.

Throughout this paper, we work in the synchronous gauge of which the line element is

$$\mathrm{d}s^2 = a^2(\eta)[-\mathrm{d}\eta^2 + (\delta_{ij} + h_{ij})\mathrm{d}x^i\mathrm{d}x^j], \tag{1}$$

where the quantities a and η are the scale factor and the conformal time, respectively. We decompose the metric perturbation into the vector and tensor modes based on the helicity basis in Fourier space:

$$h_{ij} = \sum_{\lambda=\pm1} O_{ij}^{(\lambda)} h^{(\lambda)}(\boldsymbol{k}) + \sum_{\lambda=\pm2} O_{ij}^{(\lambda)} h^{(\lambda)}(\boldsymbol{k}), \tag{2}$$

where the first and second terms represent the vector ($\lambda = \pm1$) and tensor ($\lambda = \pm2$) modes, respectively. Here we have defined

$$O_{ij}^{(\pm1)}(\hat{\boldsymbol{k}}) = \hat{k}_i \epsilon_j^{(\pm1)}(\hat{\boldsymbol{k}}) + \hat{k}_j \epsilon_i^{(\pm1)}(\hat{\boldsymbol{k}}), \tag{3}$$

$$O_{ij}^{(\pm2)}(\hat{\boldsymbol{k}}) = \epsilon_i^{(\pm1)}(\hat{\boldsymbol{k}}) \epsilon_j^{(\pm1)}(\hat{\boldsymbol{k}}), \tag{4}$$

where the polarization vectors $\boldsymbol{\epsilon}^{(\pm1)}$ satisfy the relations: $\hat{\boldsymbol{k}} \cdot \boldsymbol{\epsilon}^{(\pm1)} = 0$, $(\boldsymbol{\epsilon}^{(\pm1)})^* = \boldsymbol{\epsilon}^{(\mp1)}$, and $\boldsymbol{\epsilon}^{(\pm1)} \cdot \boldsymbol{\epsilon}^{(\mp1)} = 1$. For the vector mode, we define the gauge invariant variable in Fourier space by

$$\sigma_{ij}(\boldsymbol{k}) \equiv \sum_{\lambda=\pm1} O_{ij}^{(\lambda)} h_{ij}^{(\lambda)\prime}(\boldsymbol{k})/k, \tag{5}$$

where a prime denotes a derivative with respect to the conformal time η. With this definition, the helicity modes of σ_{ij} are given by $\sigma^{(\pm1)} = h^{(\pm1)\prime}/k$.

A. Magnetic vector and tensor modes

PMFs act as a source of the vector and tensor modes [42,44–46,89,90]. We first introduce the general property of PMFs. We then present the magnetic vector and tensor modes induced by PMFs.

1. General property of PMFs

We consider the magnetically induced vector and tensor modes presented by Refs. [42,44–46]. We assume that the time evolution of physical magnetic fields $B(a,\boldsymbol{x})$ is given by $B(a,\boldsymbol{x}) = B(\boldsymbol{x})/a^2$ with $B(\boldsymbol{x})$ being the comoving magnetic fields without the adiabatic decay due to the expansion of the Universe. This assumption is valid in the limit of infinite electrical conductivity of the Universe as in the early time.

The power spectrum of the divergence-free vector such as PMFs is given by

$$\langle B_i(\boldsymbol{k}) B_j^*(\boldsymbol{k}')\rangle = (2\pi)^3 \delta_{\rm D}^3(\boldsymbol{k}-\boldsymbol{k}') P_{ij}(\hat{\boldsymbol{k}}) P_B(k), \tag{6}$$

where $P_{ij}(\hat{\boldsymbol{k}}) = (\delta_{ij} - \hat{k}_i\hat{k}_j)/2$, and $B_i(\boldsymbol{k})$ is the Fourier transform of $B_i(\boldsymbol{x})$ given by

$$\boldsymbol{B}(\boldsymbol{x}) = \int \frac{{\rm d}^3\boldsymbol{k}}{(2\pi)^3} \boldsymbol{B}(\boldsymbol{k}) e^{i\boldsymbol{k}\cdot\boldsymbol{x}}. \tag{7}$$

We model the power spectrum of the primordial magnetic field by the power-law form (see, e.g., Ref. [91]):

$$P_B(k) = B_\lambda^2 \frac{\Gamma\left(\frac{n_B+3}{2}\right)}{4\pi^2 \lambda^{n_B+3}} k^{n_B} \Theta(k_{\rm D} - k), \tag{8}$$

where the functions $\Gamma(x)$ and $\Theta(x)$ are the gamma function and the Heaviside theta function, respectively. The quantities B_λ and $k_{\rm D}$ are the amplitude of PMFs smoothed over a comoving scale of $\lambda = 1$ Mpc and the damping scale, respectively. We introduce the Heaviside theta function to express the damping scale. We use the damping scale $k_{\rm D}$ given by Refs. [89,91,92]:

$$k_{\rm D} = (2.9\times10^4)^{\frac{1}{n_B+5}} \left(\frac{B_\lambda}{\rm nG}\right)^{-\frac{2}{n_B+5}} (2\pi)^{\frac{n_B+3}{n_B+5}} h^{\frac{1}{n_B+5}}, \tag{9}$$

with h being the reduced Hubble constant. The power spectrum of PMFs contains two parameters, B_λ and n_B. The CMB observations provide the upper limits $B_\lambda \lesssim O(1\ {\rm nG})$ depending on the value of n_B.

A key quantity for investigating the cosmological impact of PMFs is the anisotropic stress and its power spectrum. The anisotropic stress of PMFs, $\Pi_{B,ij}$, is given by

$$\Pi_{B,ij}(\boldsymbol{k}) = -\frac{1}{4\pi\rho_{\gamma,0}} \int \frac{{\rm d}^3\boldsymbol{k}_1}{(2\pi)^3} B_i(\boldsymbol{k}_1) B_j(\boldsymbol{k}-\boldsymbol{k}_1), \tag{10}$$

where $\rho_{\gamma0}$ is the photon energy density at the present time. As with the metric perturbation, we decompose the anisotropic stress into the vector and tensor components by using the helicity basis:

$$\Pi_{B,ij}(\boldsymbol{k}) = \sum_{\lambda=\pm1} O_{ij}^{(\lambda)}(\hat{\boldsymbol{k}}) \Pi_B^{(\lambda)}(\boldsymbol{k}) + \sum_{\lambda=\pm2} O_{ij}^{(\lambda)}(\hat{\boldsymbol{k}}) \Pi_B^{(\lambda)}(\boldsymbol{k}). \tag{11}$$

The power spectra of the anisotropic stress for the vector and tensor modes are then given by [42,46]

$$\langle \Pi_B^{(\lambda)}(\boldsymbol{k}) \Pi_B^{(-\lambda)}(\boldsymbol{k}')\rangle = (2\pi)^3 \delta_{\rm D}^3(\boldsymbol{k}-\boldsymbol{k}') \frac{1}{2} |\Pi_B^{(X)}|^2, \tag{12}$$

where we denote $X = V$ and $X = T$ for the vector ($\lambda = \pm1$) and tensor (±2) modes, respectively. Here we assume the unpolarized case, where the power spectra of the $+$ and $-$ modes are identical. In Eq. (12), we define

$$|\Pi_B^{(V/T)}(\boldsymbol{k})|^2 = \frac{c_{V/T}}{4(4\pi\rho_{\gamma0})^2} \int \frac{{\rm d}^3\boldsymbol{k}_1}{(2\pi)^3} \times P_B(k_1) P_B(k_2) D_{V/T}(k,k_1,\mu), \tag{13}$$

where $\boldsymbol{k}_2 = \boldsymbol{k} - \boldsymbol{k}_1$. In the above, $c_{V/T}$ are constants, $c_V = 1$ and $c_T = 1/2$, and we have defined $D_V(k,k_1,\mu) = 1\text{–}2\gamma^2\beta^2 + \gamma\beta\mu$, and $D_T(k,k_1,\mu) = (1+\gamma^2)(1+\beta^2)$, with $\mu = \hat{\boldsymbol{k}}_1 \cdot \hat{\boldsymbol{k}}_2$, $\gamma = \hat{\boldsymbol{k}} \cdot \hat{\boldsymbol{k}}_1$, $\beta = \hat{\boldsymbol{k}} \cdot \hat{\boldsymbol{k}}_2$.

The anisotropic stress defined in Eq. (10) contributes to the energy-momentum tensor in the Einstein equation, and sources the fluctuations induced magnetically. In what follows, we briefly review the resultant vector and tensor fluctuations induced by the anisotropic stress of PMFs.

2. Vector mode

We first introduce the magnetically induced vector mode. In the initial time, the anisotropic stress of PMFs is compensated by that of neutrinos. Hence, the total

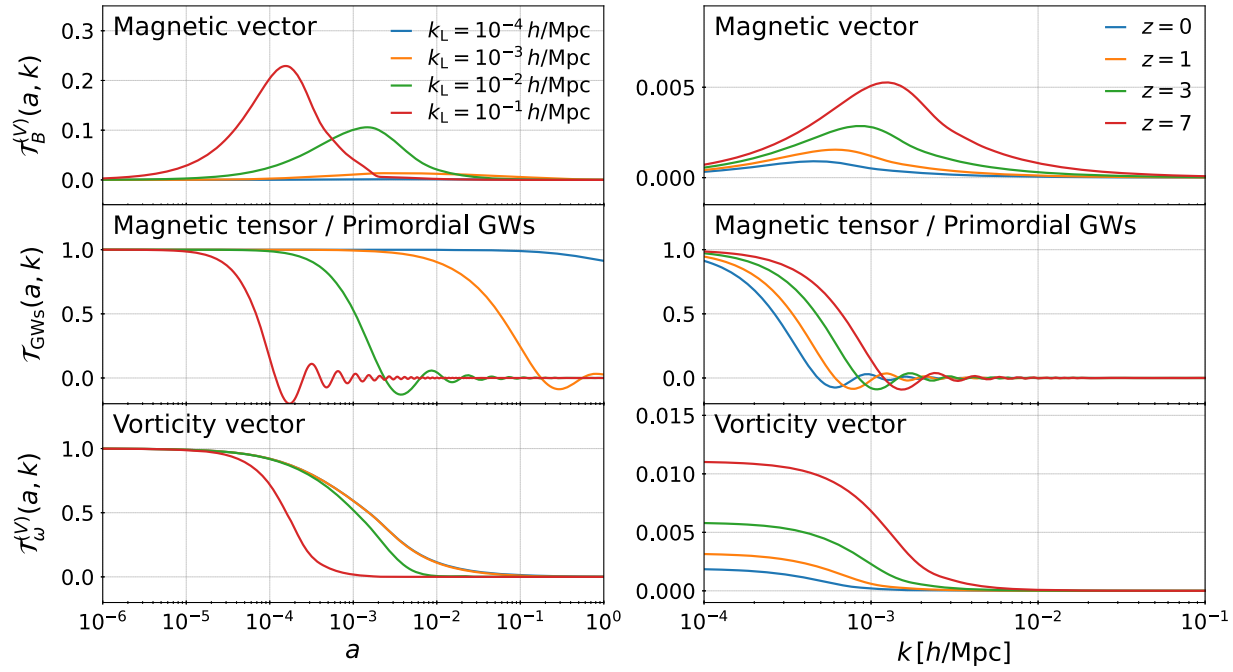

FIG. 1. Time and wave number dependences (left and right, respectively) of the transfer function. From top to bottom, we show the transfer function of the magnetic vector mode [42,89], magnetic tensor mode/primordial GWs, and vorticity vector mode [46], respectively.

anisotropic stress is zero, but each component is perturbed. In this setup, Ref. [46] has derived the initial condition for the Einstein-Boltzmann equation and shown that all the perturbed variables are proportional to $\Pi_B^{(\pm1)}(\boldsymbol{k})$ in Eq. (11) (see Appendix B in Ref. [46]). This contribution is known as *compensated vector mode*. Here, we define the transfer function of the vector mode by

$$\sigma^{(\pm1)}(\eta,\boldsymbol{k}) = \mathcal{T}_B^{(V)}(\eta,k)\Pi_B^{(\pm1)}(\boldsymbol{k}). \tag{14}$$

We note that even though the magnetic field itself is a random Gaussian variable, the statistical property of the vector mode is highly non-Gaussian, as the anisotropic stress is proportional to the square of the magnetic field.

We plot the time and wave number dependences of the transfer function in the top panels of Fig. 1. To compute the transfer function of the compensated vector mode $\mathcal{T}_B^{(V)}$, we use the CAMB code [93].[1] In the right panel, we show only the low-redshift results because we are interested in the late-time effect of PMFs on the galaxy IAs. In the limit $a \to 0$, in contrast to the usual adiabatic initial condition or primordial GW cases, the transfer function asymptotically approaches zero. This is because the vector metric perturbation is sourced by the total anisotropic stress, which however initially cancels between the magnetic field and neutrinos.

3. Tensor mode

The tensor metric perturbation arises from the anisotropic stress of PMFs after its generation time. However, after the neutrino decoupling, the contribution to the total energy-momentum tensor from the anisotropic stress of PMFs is canceled by the anisotropic stress of neutrinos. The generation of the tensor mode therefore ceases at the epoch of neutrino decoupling. This contribution is known as *passive tensor mode* [46].

The expression of the generated tensor mode is given by [46]

$$h_{\rm ini}^{(\pm2)}(\boldsymbol{k}) = 6R_\gamma \ln(\eta_\nu/\eta_B)\Pi_B^{(\pm2)}(\boldsymbol{k}), \tag{15}$$

where we define an energy fraction of photons in the total radiation defined $R_\gamma = \rho_\gamma/(\rho_\gamma+\rho_\nu)$, and the quantities η_ν and η_B are the neutrino decoupling time and the PMF generation time in terms of the conformal time, respectively. The generation epoch η_B highly depends on the generation mechanism; therefore, η_ν/η_B has an ambiguity as $10^6 \lesssim \eta_\nu/\eta_B \lesssim 10^{17}$. In the following analysis, we adopt the maximum value $\eta_\nu/\eta_B = 10^{17}$, corresponding to the grand unification energy scale [91], while the change of $h_{\rm ini}^{(\pm2)}$ (and induced E/B-mode ellipticity field appearing below) is only by a factor of < 3 even if adopting other values.

[1] In the initial parameter file for the CAMB code, we set `vector_mode = 1` to output the transfer function of the compensated vector mode.

Once the tensor metric perturbation is generated from the anisotropic stress of PMFs, it evolves as the usual primordial GWs [41,46,94]. Therefore we may express the magnetic tensor mode at the time η by using the transfer function of the primordial GWs $\mathcal{T}_{\rm GWs}(k,\eta)$ by

$$h^{(\pm 2)}(\eta,\boldsymbol{k}) = 6R_\gamma \ln(\eta_\nu/\eta_B)\mathcal{T}_{\rm GWs}(k,\eta)\Pi_B^{(\pm 2)}(\boldsymbol{k}), \quad (16)$$

where $\mathcal{T}_{\rm GWs}(k,\eta)$ stands for the transfer function of the primordial GWs as explained in the next subsection. As with the magnetic vector mode, the magnetic tensor mode is proportional to the square of PMFs, suggesting that its statistical property is highly non-Gaussian. We remark that the tensor mode arises from the same mechanism in Sec. II A 2, i.e., *compensated tensor mode*. However, its amplitude is negligible compared to the tensor mode presented in this section (see, e.g., Ref. [91]), and hence we ignore it throughout this paper.

B. Other vector and tensor sources

Here, we introduce other possible sources of vector and tensor modes: the (neutrino) vorticity vector mode and the primordial GWs. In the next section, we will compare the vector and tensor modes introduced in this subsection with those induced by PMFs.

Another possible source of a vector mode is the (neutrino) vorticity vector mode [42,46,88], in which, similar to the isocurvature initial conditions, the sum of the neutrino, baryon, and photon vorticities vanishes initially, but the vector metric perturbation remains constant due to the neutrino anisotropic stress (see Appendix 2 in Ref. [46]). Using the transfer function of the vorticity mode $\mathcal{T}_\omega^{(V)}(\eta,k)$, the vector metric perturbation at the time η is given by

$$\sigma^{(\pm 1)}(\eta,\boldsymbol{k}) = \mathcal{T}_\omega^{(V)}(\eta,k)\sigma_{\rm ini}^{(\pm 1)}(\boldsymbol{k}), \quad (17)$$

where $\sigma_{\rm ini}^{(\pm 1)}(\boldsymbol{k})$ is the primordial amplitude. We define its power spectrum by

$$\langle \sigma_{\rm ini}^{(\pm 1)}(\boldsymbol{k})\sigma_{\rm ini}^{(\mp 1)}(\boldsymbol{k}')\rangle = (2\pi)^3\delta_{\rm D}^3(\boldsymbol{k}-\boldsymbol{k}')\frac{2\pi^2}{k^3}\mathcal{P}_{\sigma^{(\pm 1)}}(k). \quad (18)$$

In the unpolarized case $\mathcal{P}_{\sigma^{(+1)}}(k) = \mathcal{P}_{\sigma^{(-1)}}(k) = \mathcal{P}_\sigma(k)/2$, where $\mathcal{P}_\sigma(k)$ stands for the total power spectrum defined by $\langle \sigma_{{\rm ini}i}(\boldsymbol{k})\sigma^*_{{\rm ini}i}(\boldsymbol{k}')\rangle = (2\pi)^3\delta_{\rm D}^3(\boldsymbol{k}-\boldsymbol{k}')(2\pi^2/k^3)\mathcal{P}_\sigma(k)$. We parametrize the total power spectrum by the power-law form:

$$\mathcal{P}_\sigma(k) = r_V\mathcal{A}_S\left(\frac{k}{k_*}\right)^{n_V}, \quad (19)$$

with $\mathcal{A}_S$ and $k_* = 0.002$ Mpc being the amplitude of the usual nonmagnetic scalar perturbation and the pivot scale. The shape of the power spectrum is controlled by the vector-to-scalar ratio r_V and spectral index n_V. Although finding a mechanism to source this mode is challenging, this initial condition is mathematically possible and has been indeed investigated by many authors, e.g., Refs. [87,95–97]. We show the behaviors of the transfer function in the middle two panels of Fig. 1 by using the CAMB code [93].[2]

Another possible source of a tensor mode is the usual primordial GWs generated during inflation from the quantum fluctuations. The tensor mode is formally given by using the transfer function $\mathcal{T}_{\rm GWs}(\eta,k)$ and initial fluctuation $h_{\rm ini}^{(\pm 2)}(\boldsymbol{k})$:

$$h^{(\pm 2)}(\eta,\boldsymbol{k}) = \mathcal{T}_{\rm GWs}(\eta,k)h_{\rm ini}^{(\pm 2)}(\boldsymbol{k}). \quad (20)$$

We define the power spectrum of the initial field by

$$\langle h_{\rm ini}^{(\pm 2)}(\boldsymbol{k})h_{\rm ini}^{(\mp 2)}(\boldsymbol{k}')\rangle = (2\pi)^3\delta_{\rm D}^3(\boldsymbol{k}-\boldsymbol{k}')\frac{2\pi^2}{k^3}\mathcal{P}_{h^{(\pm 2)}}(k). \quad (21)$$

We consider the unpolarized case $\mathcal{P}_{h^{(+2)}}(k) = \mathcal{P}_{h^{(-2)}}(k) = \mathcal{P}_h(k)/2$, where $\mathcal{P}_h(k)$ stands for total power spectrum defined by $\langle h_{{\rm ini}ij}(\boldsymbol{k})h^*_{{\rm ini}ij}(\boldsymbol{k}')\rangle = (2\pi)^3\delta_{\rm D}^3(\boldsymbol{k}-\boldsymbol{k}')(2\pi^2)/k^3\mathcal{P}_h(k)$. We model the total power spectrum of the initial field by the power-law form:

$$\mathcal{P}_h(k) = r_T\mathcal{A}_S\left(\frac{k}{k_*}\right)^{n_T}, \quad (22)$$

where r_T and n_T are the usual tensor-to-scalar ratio and spectral index, respectively. In the bottom panels in Fig. 1, we show the behaviors of the transfer function $\mathcal{T}_{\rm GWs}$ by numerically solving the evolution equation for the primordial GWs:

$$\mathcal{T}''_{\rm GWs}(\eta,k) + 2\mathcal{H}\mathcal{T}'_{\rm GWs}(\eta,k) + k^2\mathcal{T}_{\rm GWs}(\eta,k) = 0, \quad (23)$$

with the initial conditions $\mathcal{T}_{\rm GW}(0,k) = 1$ and $\mathcal{T}'_{\rm GW}(0,k) = 0$. Here, we define the conformal Hubble parameter $\mathcal{H} = a'/a$.

III. IMPACT OF THE VECTOR AND TENSOR MODES ON THE INTRINSIC ALIGNMENT

We briefly review how the vector and tensor modes induce the IAs of galaxies. We leave the detailed derivation to Appendix A.

The local physical effects of the long-wavelength vector and tensor modes on the gravitational potential have been investigated by using conformal Fermi normal coordinates in Refs. [85,98,99]. According to the results shown in Ref. [85] (or see Appendix A), the tidal fields locally

[2]We set `vector_mode = 0` to output the transfer function of the vorticity mode in the initial parameter file.

induced by the vector and tensor modes of the long-wavelength mode $k_{\rm L}$ are, respectively, given by

$$\tau_{ij}^{(V)}(\eta,k_{\rm L}) = -\frac{k_{\rm L}}{2a}(a\sigma_{ij}(\eta,k_{\rm L}))' = -\frac{k_{\rm L}}{2a}(a\mathcal{T}^{(V)}(\eta,k_{\rm L}))'\sigma_{{\rm ini}ij}(k_{\rm L}), \quad (24)$$

$$\tau_{ij}^{(T)}(\eta,k_{\rm L}) = -\frac{1}{2a}(ah'_{ij}(\eta,k_{\rm L}))' = -\frac{1}{2a}(a\mathcal{T}^{(T)\prime}(\eta,k_{\rm L}))'h_{{\rm ini}ij}(k_{\rm L}), \quad (25)$$

where we used the gauge invariant vector variable $\sigma_{ij}(k_{\rm L}) = h'_{ij}(k_{\rm L})/k_{\rm L}$. From the first line to the second line in Eqs. (24) and (25), we decompose the perturbed metric into the time-dependent part described by the transfer function and the time-independent initial part.

To derive the expression for the density field induced by the coupling between long- and short-wavelength modes, we solve the equation of motion of a matter particle in the local frame:

$$\boldsymbol{x}'' + \mathcal{H}\boldsymbol{x}' = -\boldsymbol{\nabla}_x\left(\phi_{\rm s} + \frac{1}{2}\tau_{ij}^{(X)}x^i x^j\right), \quad (26)$$

$$\nabla_x^2\phi_{\rm s} = 4\pi G a^2\bar{\rho}_{\rm m}\delta, \quad (27)$$

with $X = V$ and T for the vector and tensor modes, respectively. The quantity $\phi_{\rm s}$ stands for the scalar gravitational potential of the short-wavelength mode. To facilitate the computations, we employ the Lagrangian perturbation formalism (see Appendix A).

The second order solution arising from the short- and long-wavelength mode coupling is then given by

$$\delta^{(sl)}(\boldsymbol{x}) = \xi_{{\rm ini}ab}(k_{\rm L})\left[\left(-\frac{D^{(sl)}(\eta,k_{\rm L})}{D(\eta)} + \beta(\eta,k_{\rm L})\right) \times \partial^{-2}\partial_a\partial_b + \beta(\eta,k_{\rm L})x_a\partial_b\right]\delta^{(1)}(\boldsymbol{x},\eta), \quad (28)$$

where $\xi = \sigma$ or h for the vector or tensor modes, respectively. We define the linear growth factor $D(\eta)$, which satisfies

$$D''(\eta) + \mathcal{H}D'(\eta) - 4\pi G a^2\bar{\rho}_{\rm m}(\eta)D(\eta) = 0. \quad (29)$$

The second-order growth factor $D^{(sl)}$ satisfies

$$D^{(sl)\prime\prime} + \mathcal{H}D^{(sl)\prime} - 4\pi G a^2\bar{\rho}_{\rm m}(\eta)D^{(sl)} = S^{(X)}(\eta,k_{\rm L}), \quad (30)$$

where the source terms $S^{(X)}$ of the vector ($X = V$) and tensor ($X = T$) are, respectively, defined by

$$S^{(V)}(\eta,k_{\rm L}) = -\frac{k_{\rm L}}{2a}D(\eta)(a\mathcal{T}^{(V)}(\eta,k_{\rm L}))', \quad (31)$$

$$S^{(T)}(\eta,k_{\rm L}) = -\frac{1}{2a}D(\eta)(a\mathcal{T}^{(T)\prime}(\eta,k_{\rm L}))'. \quad (32)$$

Equation (28) allows us to estimate how the IA is induced by the long-wavelength vector and tensor modes. We use the same ansatz in Ref. [85], in which we assume that the first term in the square brackets in Eq. (28) induces the intrinsic galaxy shape, and the conversion from the second-order density fluctuations to the intrinsic galaxy shape in the vector and tensor modes has the same scaling as that in the scalar mode [85,86] (see Appendix A for details). Finally, we have the expression of the intrinsic galaxy shape induced by the long-wavelength vector and tensor modes at the linear order given by

$$\gamma_{ij}(\boldsymbol{k}) = b_{\rm K}(\eta,k)\xi_{{\rm ini}ij}(\boldsymbol{k}), \quad (33)$$

where $\xi = \sigma$ or h for the vector or tensor modes, respectively. Here we define the effective linear shape bias by

$$b_{\rm K}(\eta,k) \equiv \frac{7}{4}\left(-\frac{D^{(sl)}(\eta,k)}{D(\eta)} + \beta(\eta,k)\right)b_{\rm K}^{\rm scalar}. \quad (34)$$

The quantity $b_{\rm K}^{\rm scalar}$ is the linear shape bias induced by the scalar tides as in Ref. [86]. We omit the subscript $_{\rm L}$ indicating the long-wavelength mode here.

In Fig. 2, we show the behaviors of the effective linear shape bias parameter $b_{\rm K}(\eta,k)/b_{\rm K}^{\rm scalar}$. We notice that the effective linear shape bias sourced by the vector mode has the opposite sign to that by the tensor mode because of the different number of time derivatives in the sources [see Eqs. (31) and (32)]. Taking the limit $k \to \infty$, the transfer function asymptotically approaches zero (see the right panels in Fig. 1). However the effective tidal bias parameter does not vanish in the same limit, known as the fossil effect [85]. Since the transfer function of the vector modes decays rapidly after the matter-radiation equality, the effective linear shape bias parameter induced by the vector mode, a fossil effect, is more quickly frozen than that by the tensor mode. Therefore, we do not see the redshift dependence of the effective tidal bias parameter in the top and bottom panels in Fig. 2. We note that, since the amplitude of the effective linear shape bias parameter is solely determined by the behavior of the transfer function, its amplitude can be larger than the linear shape bias induced by the scalar tides as seen in the vector mode cases. However, the net impact of the vector mode on the galaxy shape is generally much smaller than the scalar one.

While Eq. (33) is estimated based on the ansatz we mentioned before, it is nontrivial whether Eq. (33) actually holds in the presence of long-wavelength vector/tensor modes. However, a recent numerical work [86] has

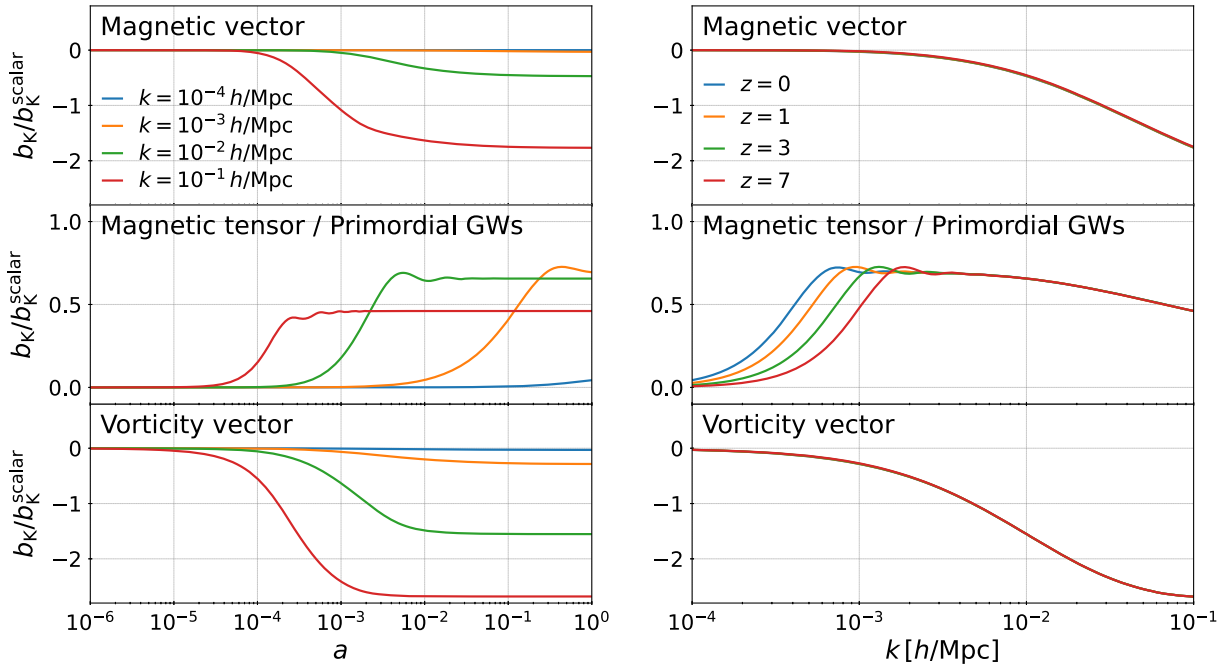

FIG. 2. Time and wave number dependences of the effective bias parameter normalized by the scalar tidal bias $b_{\rm K}/b_{\rm K}^{\rm scalar}$ (left and right, respectively). From top to bottom, we show the magnetic vector mode, magnetic tensor mode/primordial GWs, and vorticity vector mode, respectively.

investigated the validity of Eq. (33) in the primordial GW case, and confirmed that Eq. (33) agrees with simulations at large scales. Although they also confirmed that the discrepancy between the ansatz and measurements becomes larger at smaller scales, this discrepancy does not qualitatively affect the estimates in this paper, and henceforth, we will carry out the analysis assuming that Eq. (33) is valid for both the vector and the tensor modes. Numerical validation, especially for the vector mode, would be an interesting future work.

IV. THREE-DIMENSIONAL E- AND B-MODE POWER SPECTRA

From here, we move to the heart of this work, which involves the investigation of the three-dimensional power spectrum of the IA induced by the vector and tensor modes. While the vector and tensor can generally contribute to the lens-induced ellipticity (e.g., Refs. [100–104]), as we are interested in the characteristic signature of the intrinsic galaxy shapes from the magnetically induced vector and tensor modes, we simply ignore the lens-induced ellipticity but focus on the intrinsic ellipticity.

The E- and B-mode decomposition is convenient to distinguish the impact of vector and tensor modes on the galaxy shape from that of the scalar mode because the leading-order scalar mode does not induce the B mode. There however exists a scalar-mode contribution to the B mode arising from the one-loop effect, which we will properly take into account in a later section.

We work under the plane-parallel limit and set the line-of-sight direction to be parallel to the z axis: $\hat{\boldsymbol{n}} = \hat{\boldsymbol{z}}$. We define the shear E-mode and B-mode by

$$ {}_{\pm2}\gamma(\boldsymbol{k}) e^{\mp 2i\phi_k} = E(\boldsymbol{k}) \pm iB(\boldsymbol{k}), \tag{35}$$

where we define

$$ {}_{\pm2}\gamma(\boldsymbol{k}) = m_{\mp}^i m_{\mp}^j \gamma_{ij}(\boldsymbol{k}), \tag{36}$$

with $\boldsymbol{m}_\lambda = (1, -\lambda i, 0)/\sqrt{2}$. Recall the expression of the induced galaxy shape by the long-wavelength vector and tensor modes in Eq. (33):

$$\begin{aligned} \gamma_{ij} &= b_{\rm K}(k)\xi_{{\rm ini}ij}(k), \\ &= b_{\rm K}(k)\sum_\lambda O_{ij}^{(\lambda)}(\hat{\boldsymbol{k}})\xi_{\rm ini}^{(\lambda)}(\boldsymbol{k}), \end{aligned} \tag{37}$$

where $\xi = \sigma$ and h for the vector and tensor modes, respectively. Here and hereafter we omit the time dependence of $b_{\rm K}$ to simplify the notation. Using this expression, we obtain

$$ {}_{\pm2}\gamma^{(V)} = \frac{b_{\rm K}(k)}{\sqrt{2}} \sum_{\lambda=\pm1} \sigma^{(\lambda)} \sin\theta_k (\pm\lambda + \cos\theta_k) e^{\pm 2i\phi_k}, \tag{38}$$

$$ {}_{\pm2}\gamma^{(T)} = \frac{b_{\rm K}(k)}{4} \sum_{\lambda=\pm2} h^{(\lambda)} [(1+\cos^2\theta_k) \pm 2\lambda\cos\theta_k] e^{\pm 2i\phi_k}, \tag{39}$$

where the superscripts (V) and (T) stand for the vector and tensor modes, respectively. The function $b_{\rm K}(\eta,k)$ depends on the source of the vector and tensor modes (see Fig. 2).

For later purposes, we mention the nonmagnetic scalar mode tidal effect. We adopt the linear alignment model, in which the galaxy ellipticity is linearly related to the real space density field:

$$\gamma_{ij} = b_{\rm K}^{\rm scalar}\left(\hat{k}_i\hat{k}_j - \frac{1}{3}\delta_{ij}\right)\delta_{\rm L}(\boldsymbol{k}). \tag{40}$$

Substituting Eq. (40) into Eq. (36), we have

$${}_{\pm2}\gamma^{(S)} = \frac{1}{2}b_{\rm K}\sin^2\theta_k\delta_{\rm L}(\boldsymbol{k})e^{\pm2i\phi_k} \tag{41}$$

for the scalar mode.

Using Eqs. (38), (39), and (41), the expressions of the E- and B-modes are given by

$$E^{(S)}(\boldsymbol{k},\hat{\boldsymbol{n}}) = \frac{1}{2}b_{\rm K}^{\rm scalar}\sin^2\theta_k\delta_{\rm L}(\boldsymbol{k}), \tag{42}$$

$$B^{(S)}(\boldsymbol{k},\hat{\boldsymbol{n}}) = 0, \tag{43}$$

$$E^{(V)}(\boldsymbol{k},\hat{\boldsymbol{n}}) = \frac{1}{\sqrt{2}}b_{\rm K}(k)\sin\theta_k\cos\theta_k\sum_{\lambda=\pm1}\sigma^{(\lambda)}(\boldsymbol{k}), \tag{44}$$

$$B^{(V)}(\boldsymbol{k},\hat{\boldsymbol{n}}) = -\frac{i}{\sqrt{2}}b_{\rm K}(k)\sin\theta_k\sum_{\lambda=\pm1}\lambda\sigma^{(\lambda)}(\boldsymbol{k}), \tag{45}$$

$$E^{(T)}(\boldsymbol{k},\hat{\boldsymbol{n}}) = \frac{1}{4}b_{\rm K}(k)(1+\cos^2\theta_k)\sum_{\lambda=\pm2}h^{(\lambda)}(\boldsymbol{k}), \tag{46}$$

$$B^{(T)}(\boldsymbol{k},\hat{\boldsymbol{n}}) = -\frac{i}{2}b_{\rm K}(k)\cos\theta_k\sum_{\lambda=\pm2}\frac{\lambda}{2}h^{(\lambda)}(\boldsymbol{k}), \tag{47}$$

where the superscripts (S), (V), and (T) stand for the scalar, vector, and tensor modes, respectively.

As the observable quantity, we focus on the three-dimensional power spectrum, which is defined as

$$\langle X(\boldsymbol{k})Y^*(\boldsymbol{k}')\rangle = (2\pi)^3\delta_{\rm D}^3(\boldsymbol{k}-\boldsymbol{k}')P_{XY}(\boldsymbol{k}), \tag{48}$$

where $X, Y = E$ or B for the E- and B- mode power spectra. From Eqs. (42)–(47), we finally obtain

$$P_{EE}^{(S)}(k,\mu) = \frac{1}{4}(b_{\rm K}^{\rm scalar})^2(1-\mu^2)^2P_{\rm L}(k), \tag{49}$$

$$P_{BB}^{(S)}(k,\mu) = 0, \tag{50}$$

$$P_{EE}^{(V)}(k,\mu) = \frac{1}{2}(b_{\rm K}(k))^2(1-\mu^2)\mu^2P_\sigma(k), \tag{51}$$

$$P_{BB}^{(V)}(k,\mu) = \frac{1}{2}(b_{\rm K}(k))^2(1-\mu^2)P_\sigma(k), \tag{52}$$

$$P_{EE}^{(T)}(k,\mu) = \frac{1}{16}(b_{\rm K}(k))^2(1+\mu^2)^2P_h(k), \tag{53}$$

$$P_{BB}^{(T)}(k,\mu) = \frac{1}{4}(b_{\rm K}(k))^2\mu^2P_h(k), \tag{54}$$

where we define $\mu = \cos\theta_k$. The linear matter power spectrum of the density field $\delta_{\rm L}$ is given by

$$\langle\delta_{\rm L}(\boldsymbol{k})\delta_{\rm L}^*(\boldsymbol{k}')\rangle = (2\pi)^3\delta_{\rm D}^3(\boldsymbol{k}-\boldsymbol{k}')P_{\rm L}(k). \tag{55}$$

The nonvanishing EB power spectrum appears in the chiral vector and tensor modes:

$$P_{EB}^{(V)}(k,\mu) = \frac{i}{2}(b_{\rm K}(k))^2\mu(1-\mu^2)\chi_\sigma(k)P_\sigma(k), \tag{56}$$

$$P_{EB}^{(T)}(k,\mu) = \frac{i}{8}(b_{\rm K}(k))^2\mu(1+\mu^2)\chi_h(k)P_h(k), \tag{57}$$

where we define a chiral parameter $\chi_{\sigma/h}(k)$ as

$$\chi_\sigma(k) = \frac{P_{\sigma^{(+1)}} - P_{\sigma^{(-1)}}}{P_\sigma(k)}, \tag{58}$$

$$\chi_h(k) = \frac{P_{h^{(+2)}} - P_{h^{(-2)}}}{P_h(k)}. \tag{59}$$

The EB spectrum is an interesting probe for testing parity-violating theories. Hereafter, we consider unpolarized cases, $\chi_{\sigma/h}(k) = 0$.

We note that $P_{EE}^{(S)}$ is the nonmagnetic scalar contribution, but affects the detectability of PMFs by forming the E-mode covariance of the Fisher matrix (67). Moreover, at one-loop order, the density field can source the B mode, forming $P_{BB}^{(S)}$ (see Fig. 3 and Appendix B) and hence the B-mode covariance. We will also take them into account in the later Fisher matrix analysis. For the vector and tensor power spectra $P_{\sigma/h}$, we adopt (see Sec. II for details)

$$P_\sigma(k;B_\lambda,n_B) = |\Pi^{(V)}|^2, \tag{60}$$

$$P_h(k;B_\lambda,n_B) = \left(6R_\gamma\ln\left(\frac{\eta_\nu}{\eta_B}\right)\right)^2|\Pi^{(T)}|^2, \tag{61}$$

$$P_\sigma(k;r_{\rm V},n_{\rm V}) = \frac{2\pi^2}{k^3}r_{\rm V}\mathcal{A}_{\rm s}\left(\frac{k}{k_*}\right)^{n_{\rm V}}, \tag{62}$$

$$P_h(k;r_{\rm T},n_{\rm T}) = \frac{2\pi^2}{k^3}r_{\rm T}\mathcal{A}_{\rm s}\left(\frac{k}{k_*}\right)^{n_{\rm T}}, \tag{63}$$

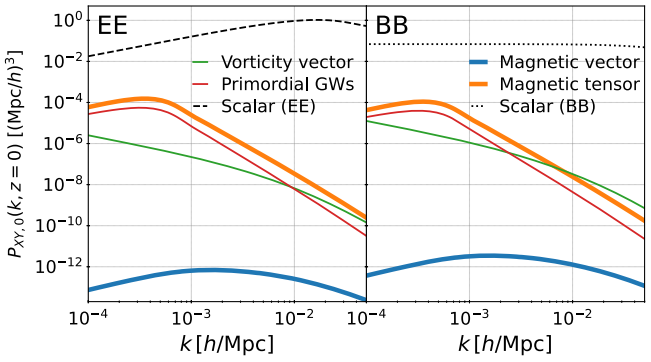

FIG. 3. E-mode (left) and B-mode (right) monopole power spectra at $z = 0$ for various sources: the magnetic vector (blue), magnetic tensor (orange), vorticity vector (green) modes, and primordial GWs (red). To compute each case, we adopt $(B_\lambda, n_B) = (2\ \mathrm{nG}, -2.9)$, $(r_\mathrm{V}, n_\mathrm{V}) = (0.01, 0)$, and $(r_\mathrm{T}, n_\mathrm{T}) = (0.03, -r_\mathrm{T}/8)$. Dashed and dotted lines represent, respectively, the E-mode power spectrum induced by the primary nonmagnetic scalar mode given in Eq. (49) and the B-mode power spectrum induced by the one-loop contribution from the scalar mode, calculated based on Ref. [105] (see Appendix B).

for the magnetic vector, magnetic tensor, vorticity vector modes, and primordial GWs, respectively.

As a demonstration, we present the lowest order multipole, the monopole, of the various models in Fig. 3, although the nonvanishing quadrupole and hexadecapole are also observables. We define the monopole by

$$P_{XX,0}(k) = \frac{1}{2}\int_{-1}^{1} \mathrm{d}\mu P_{XX}(k,\mu). \tag{64}$$

In this plot, we set the model parameters as follows: $(B_\lambda, n_B) = (2\ \mathrm{nG}, -2.9)$ taken from the upper limit by Planck results [91], $(r_\mathrm{V}, n_\mathrm{V}) = (0.01, 0)$ roughly corresponding to the upper limit obtained by using the WMAP results [95], and $(r_\mathrm{T}, n_\mathrm{T}) = (0.03, -r_\mathrm{T}/8)$ from the Planck results [106]. Also, we calculate the scalar shape bias parameter $b_\mathrm{K}^\mathrm{scalar}$ by using the fitting formula [107]:

$$b_\mathrm{K}^\mathrm{scalar} = \frac{0.09302 - 0.1289 b_1^\mathrm{E}}{1 + 0.3541 b_1^\mathrm{E}}, \tag{65}$$

where b_1^E is a linear density bias parameter. In this plot, we use the same linear density bias parameter as the hydrogen line (HI) galaxies in SKA2 [108]:

$$b_1^\mathrm{E} = c_4 e^{c_5 z}, \tag{66}$$

with $c_4 = 0.554$ and $c_5 = 0.783$. For comparison purposes, we show the contributions from the scalar mode to the E- and B-mode power spectra. While the leading-order effect of the scalar mode results only in the E mode, the one-loop order effect produces the nonvanishing B-mode contributions (e.g., Refs. [109,110]). To compute the one-loop contribution to the B-mode spectrum, we exploit the effective-theory description of galaxy shape based on Ref. [105]. See Appendix B for details.

Recalling that all the primordial power spectra are modeled by the power-law form, the characteristic feature observed in each power spectrum comes from the shape of each effective linear shape bias b_K. The power spectrum of the magnetic tensor mode has a similar behavior to that of the primordial GWs as both $n_B = -2.9$ and $n_\mathrm{T} = -0.00375$ impose nearly scale invariance of their initial power spectra P_h, and also their b_K are exactly the same. Compared to the nonmagnetic scalar power spectrum, the vector and tensor mode signals are suppressed at small scales because of the feature of the fossil effect, i.e., the absence of growth at late time.

We notice that the signal of the magnetic vector mode is 3–8 orders of magnitude smaller, depending on the scale, than those by other sources. We elaborate on the origin of this suppression as follows. First, to compute each spectrum in Fig. 3 we set the model parameters to the CMB limits; thus, the amplitude of each mode essentially reflects the amplitude of corresponding metric perturbation at around the recombination epoch. Indeed, there is a 2–4 order of magnitude gap between the magnetic vector mode and the other three in the metric perturbation, inducing a comparable gap in the IA. Second, recalling the behavior of the effective linear shape bias in the magnetic vector mode (see the right panel in Fig. 2), the effective tidal bias asymptotically approaches zero more quickly than other modes at large scales. This asymptotic behavior leads to further suppression in the magnetic vector mode at large scales. The above two facts explain the behavior illustrated in Fig. 3.

In Fig. 4, we investigate the behavior of E- and B-mode power spectra of the magnetic modes by varying the model parameters B_λ and n_B. Since we plot the signal normalized by $(B_\lambda/\mathrm{nG})^4$, the solid and dashed lines overlap if the P_{EE} and P_{BB} scale as $\propto B_\lambda^4$. We indeed see this feature for $n_B \lesssim -1.5$, while their gap increases as n_B gets larger than -1.5. This is because, for the blue tilted case, a convolution integral in the anisotropic stress (10) becomes more sensitive to the ultraviolet magnetic cutoff k_D depending on B_λ [see Eq. (9)], and hence the power spectrum of the anisotropic stress no longer obeys a simple B_λ^4 scaling (see, e.g., Refs. [44,45,111]). Corresponding to the change of the impact of k_D at $n_B \sim -1.5$, the dependence of P_{EE} and P_{BB} on n_B also changes, i.e., they decrease for small n_B but start increasing as n_B enlarges. As a consequence, they are minimized at $n_B \sim -1.5$. This unique feature straightforwardly determines the dependence of the detectability of B_λ on n_B as shown in Figs. 5 and 6. The overall amplitude of the tensor mode is larger than that of the vector mode due to the prefactor $(6R_\gamma \ln(\eta_\nu/\eta_B))^2 \approx 2 \times 10^4$. As we will demonstrate in the next section, the contribution from the tensor

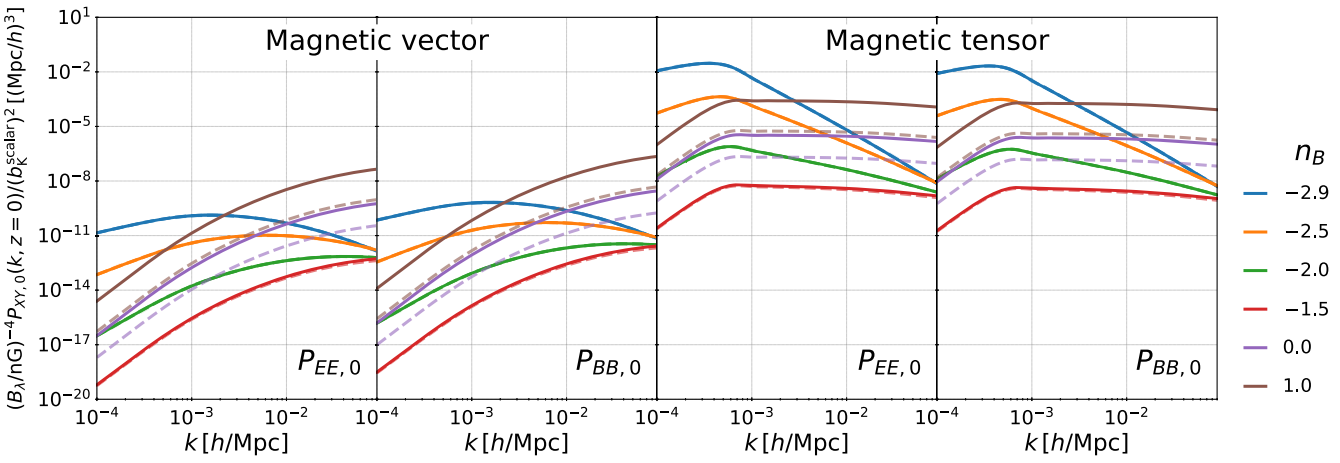

FIG. 4. E- and B-mode power spectra induced by PMFs normalized by $(B_\lambda/\mathrm{nG})^4$ at $z=0$. Left two and right two panels, respectively, show the magnetic vector and magnetic tensor modes. Solid and dashed lines show the results in $B_\lambda = 1.0$ and 10 nG, respectively.

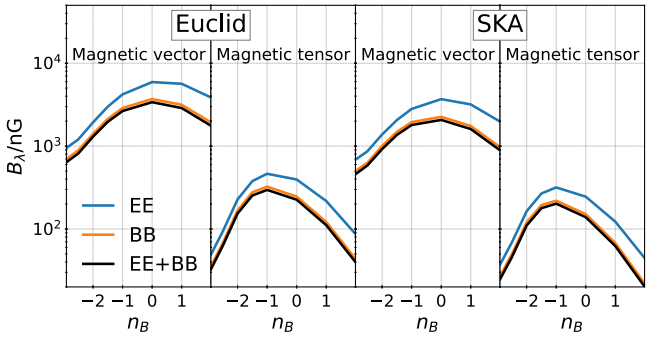

FIG. 5. Minimum detectable value for the Euclid spectroscopic survey (left two panels) and SKA HI galaxy surveys (right two panels) obtained through the magnetic vector mode and through the magnetic tensor mode as indicated. Blue, orange, and black lines, respectively, show the results obtained by E-mode power spectrum alone, by B-mode power spectrum alone, and by combining E- and B-mode power spectra, respectively. We note that the orange and black lines, corresponding to the results from B mode alone and from both E and B modes, respectively, almost overlap, showing that the B mode gives a much larger gain than the E mode. For visualization purposes, we multiply the B-mode results by a factor of 1.12.

mode is an important source in constraining PMFs through the observation of the IA of galaxies.

V. FISHER FORECAST

In this section, we discuss the constraining power of the E- and B-mode power spectra of the galaxy shape on the amplitude of PMFs based on the analytic model given in Eqs. (51)–(54) with Eqs. (60) and (61). To this end, we perform a Fisher matrix analysis. Following, e.g., Ref. [72], we define the Fisher matrix for the parameter vector $\boldsymbol{\theta}$ as

$$F_{ij} = \frac{V}{(2\pi)^2}\int_{k_{\min}}^{k_{\max}} k^2 \mathrm{d}k \int_{-1}^{1} \mathrm{d}\mu \times \sum_{a,b=EE,BB}\left(\frac{\partial P_a}{\partial \theta_i}\right)[\mathrm{cov}^{-1}]_{ab}\left(\frac{\partial P_b}{\partial \theta_j}\right), \quad (67)$$

where the quantity V represents the survey volume. The covariance matrix cov_{ab} is given by

$$\mathrm{cov}_{ab} = 2\left(P_a + \frac{\sigma_\gamma^2}{n_{\mathrm{gal}}}\right)^2 \delta_{a,b}, \quad (68)$$

with σ_γ and n_{gal} being the root mean square of the galaxy's ellipticity and the galaxy number density, respectively.

Our analysis examines the constraints on the amplitude of PMFs, B_λ with a fixed spectral index n_B. In this case, the expression of the Fisher matrix is reduced to

$$F(B_{\lambda,\mathrm{fid}}) = \frac{V}{2(2\pi)^2}\int_{k_{\min}}^{k_{\max}} k^2 \mathrm{d}k \int_{-1}^{1} \mathrm{d}\mu \times \sum_{a=EE,BB}\left(\frac{\partial P_a}{\partial B_\lambda}\frac{1}{P_a + \sigma_\gamma^2/n_{\mathrm{gal}}}\bigg|_{B_\lambda = B_{\lambda,\mathrm{fid}}}\right)^2, \quad (69)$$

with $B_{\lambda,\mathrm{fid}}$ being the fiducial value of the parameter. The size of the expected error on the PMF strength is given by $\sigma(B_{\lambda,\mathrm{fid}}) = \sqrt{F^{-1}(B_{\lambda,\mathrm{fid}})}$. PMFs whose strength exceeds the size of the error are detectable at the 1σ level; thus, a minimum detectable value of the PMF strength $B_{\lambda,\min}$ is given by a solution of the equation

$$\sigma(B_{\lambda,\min}) = B_{\lambda,\min}. \quad (70)$$

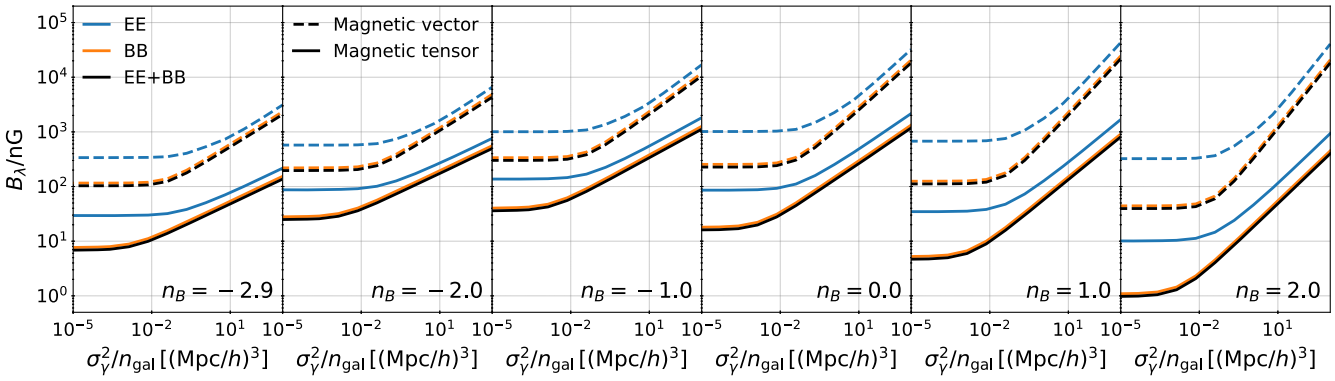

FIG. 6. Minimum detectable value for the idealistic surveys by varying $\sigma_\gamma^2/n_{\rm gal}$, obtained through the magnetic vector mode (dashed lines) and through the magnetic tensor mode (solid lines). We present the results obtained by the E-mode power spectrum alone (blue), by the B-mode power spectrum alone (orange), and by combining the E- and B-mode power spectra (black). The orange and black lines, corresponding to the results from the B mode only and from both the E and B modes, respectively, almost overlap, showing that the B mode gives a much bigger gain than the E mode. For visualization purposes, we multiply the B-mode results by a factor of 1.12.

Throughout the analysis, we incorporate the E-mode power spectrum induced by the scalar mode and the B-mode power spectrum induced by the vector and tensor modes and the one-loop contribution from the scalar mode into the Fisher analysis. In computing the one-loop B-mode spectrum, we follow Ref. [105] and use the effective-theory description of galaxy shape (see Appendix B for details). We set $k_{\rm min} = 2\pi V^{-1/3}$, $k_{\rm max} = 0.1$ Mpc$/h$, and $\sigma_\gamma = 0.3$. The scalar shape bias parameter $b_{\rm K}^{\rm scalar}$ is calculated by using the fitting formula [107] given in Eq. (65).

We first demonstrate the expected minimum detectable value for the Euclid spectroscopic survey [112] and SKA [113]. The galaxy redshift surveys by Euclid and SKA will, respectively, observe the Hα emitter over redshifts 0.9 to 1.8 and HI galaxies over redshifts 0.23 to 1.81. Although IA has not yet been detected for emission line galaxies (ELGs) [64,114–116], Ref. [117] recently proposed an optimal estimator to determine the IA of halos using ELGs. We suppose that the power spectra related to the IA can be measured with the optimal estimator, and that all observed ELGs are, therefore, an ideal tracer of the halo shape. We use the survey specifications in Table 3 of Ref. [118] for the Euclid and Table 1 of Ref. [119] for SKA. We combine all the redshift bins by $\sigma(B_\lambda) = 1/\sqrt{\sum_i F(B_\lambda)|_{z=z_i}}$ with the subscript i being the label of the redshift bins, and then numerically solve Eq. (70). In Fig. 5, we present the minimum detectable value for Euclid and SKA (see Appendix C for the same analysis but for the vorticity vector mode and primordial GWs). As expected from Fig. 4, the magnetic tensor mode provides stronger constraints on the PMF strength than the magnetic vector mode. It is also apparent from Fig. 5 that the B-mode power spectrum places stronger constraints than the E-mode power spectrum due to the absence of the sizable nonmagnetic scalar contribution in the covariance matrix. We find that $B_{\lambda,\rm min}$ has a local maximum around $n_B \sim -1$. This behavior comes from a unique n_B dependence of P_{EE} and P_{BB} seen in Fig. 4 and the lower limit of the integration range in the Fisher matrix for the survey specification of Euclid/SKA $k_{\rm min} = 2\pi V^{-1/3} \approx 0.001\ h/$Mpc. One can find from Fig. 5 that PMFs with $B_\lambda \sim 30$–300 nG would be measurable by a Euclid- or SKA-level B-mode survey.

To capture PMFs with $B_\lambda = \mathcal{O}(1$ nG$)$, what specific level of survey should be aimed at? To figure this out, we compute the minimum detectable value $B_{\lambda,\,\rm min}$ by varying the shot noise contribution to the covariance matrix $\sigma_\gamma^2/n_{\rm gal}$ (see Appendix C for the same analysis but for the vorticity vector mode and primordial GWs). We then set $V = 1({\rm Gpc}/h)^3$ and $z = 1.0$. We also use the same bias parameter as the HI galaxies in SKA2 given in Eq. (66). The choice of these parameters does not qualitatively change the results. Figure 6 describes our results, again showing that the B-mode information induced by the tensor mode is the most powerful to measure B_λ. Both for the E-mode and B-mode cases, decreasing the shot noise level causes the dominance of the nonmagnetic scalar signal in the covariance and hence the saturation of $B_{\lambda,\,\rm min}$ around $\sigma_\gamma^2/n_{\rm gal} \sim 10^{-2}$. We finally find that the saturated value of $B_{\lambda,\,\rm min}$ reaches $\mathcal{O}(1$ nG$)$–$\mathcal{O}(10$ nG$)$, depending on the spectral index. To archive this minimum detectable value, the B-mode power spectrum plays a major role and still an interesting probe even in the presence of the one-loop nonmagnetic scalar contribution to the B mode.

VI. SUMMARY

In recent years, there has been growing attention on PMFs as a strong candidate for explaining the origin of observed large-scale magnetic fields, including void regions. While the statistical properties of PMFs have been constrained by the recent cosmological observations such as the cosmic microwave background anisotropies, this

paper has focused on the IAs of galaxies as a complementary new observational probe, aiming to delve into the nature of PMFs. The metric perturbations of the long-wavelength vector and tensor modes are known to induce the local tidal gravitational fields [85]. Through the observations of the intrinsic galaxy shapes, we have paved the way to detect the vector and tensor modes sourced by the anisotropic stress of PMFs in the early Universe.

We have shown the relation between the anisotropic stress of PMFs and the IA of the galaxies. Considering up to the leading-order contributions, while the scalar mode only produces the cosmic shear E mode, the vector and tensor modes produce both E and B modes. Hence, the B-mode signal can be a good probe to search for magnetically induced vector and tensor modes once we properly take into account the one-loop scalar contribution to the B mode. Assuming that the power spectrum of PMFs is given by a power-law function, which includes two parameters, the amplitude of PMFs B_λ and the spectral index n_B, we demonstrated the E- and B-mode power spectra of the galaxy shape induced by PMFs. Owing to the convolution and small-scale cutff inherent in the anisotropic stress of PMFs, we found that the slopes of the E- and B-mode spectra do not change for $n_B > -1.5$ as n_B is increased, but only their amplitudes vary with n_B.

Based on our analytical model of the E- and B-mode spectra, we have performed the Fisher analysis to estimate the minimum detectable value of the PMF strength, defined in Eq. (70), for a fixed spectral index. We first examined the minimum detectable value assuming the galaxy redshift survey by Euclid and SKA. In this case, we found that the minimum detectable value of B_λ reaches about 30–300 nG, depending on n_B, which is weaker than the upper limit obtained by the recent CMB observations. To investigate the detecting power of the IA observations in spectroscopic surveys, we further performed the Fisher matrix analysis by varying the shot noise term as a free parameter. We found that a minimum detectable value can reach $\mathcal{O}(1\ \mathrm{nG})$–$\mathcal{O}(10\ \mathrm{nG})$, depending on n_B, which is almost comparable to the current CMB limits, and that the B-mode spectrum still plays a crucial role in achieving this even in the presence of the nonmagnetic scalar contribution to the B mode spectrum. The currently planned galaxy redshift surveys would provide weaker constraints on PMFs than the CMB observations. However, the observations of the galaxy IAs would become increasingly important as a complementary probe to understand the nature of PMFs.

This paper has focused on the auto power spectra of the cosmic shear E and B modes induced by PMFs. However, as the anisotropic stress of PMFs also induces the density fluctuations [46], we would observe a nonvanishing signal in the cross-correlation between density fields and galaxy shapes. Adding this information to the present analysis would improve the constraint on PMFs. An interesting future challenge is to probe PMFs, making comprehensive use of the available information on the galaxy density field and its shape.

We have carried out our analysis with a spectroscopic survey in mind. When considering an analysis based on the two-dimensional angular power spectrum for a photometric survey (e.g., Ref. [87]), we expect that the impact of the shot noise on the covariance is reduced due to the larger number density of galaxies than spectroscopic surveys. We leave detailed comparisons of the detecting power on PMFs between the two-dimensional angular power spectrum and three-dimensional power spectrum for an intriguing future work.

ACKNOWLEDGMENTS

S. S. and K. A. are supported by JSPS Overseas Research Fellowships. This work is supported by the Japan Society for the Promotion of Science (JSPS) KAKENHI Grants No. JP23K19050 (S. S.), No. JP20H05859 (M. S.), and No. JP23K03390 (M. S.). K. A. also acknowledges support from Fostering Joint International Research (B) under Contract No. 21KK0050. T. O. acknowledges support from the Ministry of Science and Technology of Taiwan under Grants No. MOST 111-2112-M-001-061- and No. NSTC 112-2112-M-001-034- and the Career Development Award, Academia Sinica (No. AS-CDA-108-M02) for the period of 2019–2023.

APPENDIX A: INTRINSIC ALIGNMENTS FROM VECTOR AND TENSOR MODES

In this appendix, based on Ref. [85], we solve the equation of motion of a matter particle in a local frame in the presence of the local tidal effect, and then derive the density fields induced by the crosstalk between the long- and short-wavelength modes. From the expression for the second-order density fields, we show the linear shape bias of the IA of galaxies from the vector and tensor modes.

Our starting point is the expression of the tidal field induced by the long-wavelength vector and tensor modes using conformal Fermi normal coordinate [85]

$$\tau_{ij}(\eta, k_{\mathrm{L}}) = -\frac{1}{2a}(a h'_{ij}(\eta, k_{\mathrm{L}}))', \tag{A1}$$

where we work in the synchronous gauge. It is useful to decompose the tidal tensor into the time-dependent part and initial perturbation part:

$$\tau_{ij}(\eta, k_{\mathrm{L}}) = \mathcal{T}_\tau(\eta, k_{\mathrm{L}})\xi_{\mathrm{ini}ij}(k_{\mathrm{L}}), \tag{A2}$$

where $\xi = \sigma$ and h for the vector and tensor modes, respectively. The function $\mathcal{T}_\tau(\eta, k_{\mathrm{L}})$ is given by

$$\mathcal{T}_\tau(\eta, k_{\mathrm{L}}) = -\frac{k_{\mathrm{L}}}{2a}(a\mathcal{T}^{(V)}(\eta, k_{\mathrm{L}}))' \tag{A3}$$

for the vector mode, and

$$\mathcal{T}_\tau(\eta, k_{\rm L}) = -\frac{1}{2a}(a\mathcal{T}^{(T)\prime}(\eta, k_{\rm L}))' \tag{A4}$$

for the tensor mode.

In the presence of the long-wavelength tidal tensor τ_{ij}, the equation of motion of a matter particle in the local frame becomes

$$\boldsymbol{x}'' + \mathcal{H}\boldsymbol{x}' = -\boldsymbol{\nabla}_x\left(\phi_{\rm s} + \frac{1}{2}\tau_{ij}x^i x^j\right), \tag{A5}$$

$$\nabla_x^2\phi_{\rm s} = 4\pi G a^2\bar{\rho}_{\rm m}\delta, \tag{A6}$$

where a prime denotes a derivative with respect to the conformal time η. To solve the equation of motion, we employ the Lagrangian perturbation formalism. The Lagrangian description relates the initial Lagrangian position for the fluid element $\boldsymbol{q}$ to the Eulerian position at conformal time η through the displacement field $\boldsymbol{\Psi}(\eta, \boldsymbol{q})$:

$$\boldsymbol{x}(\eta, \boldsymbol{q}) = \boldsymbol{q} + \boldsymbol{\Psi}(\eta, \boldsymbol{q}). \tag{A7}$$

Substituting Eq. (A7) into Eq. (A5), the equation for $\boldsymbol{\Psi}$ at the first order is given by

$$\boldsymbol{\Psi}'' + \mathcal{H}\boldsymbol{\Psi}' = -\boldsymbol{\nabla}_q\left(\phi_{\rm s}(\boldsymbol{q}) + \frac{1}{2}\tau_{ij}q^i q^j\right). \tag{A8}$$

We split the displacement field into the long- and short-wavelength mode contributions:

$$\boldsymbol{\Psi} = \boldsymbol{\Psi}^{(s)} + \boldsymbol{\Psi}^{(l)}. \tag{A9}$$

The evolution equation of each displacement field is given by

$$\Psi_i^{(s)\prime\prime} + \mathcal{H}\Psi_i^{(s)\prime} = -\frac{\partial\phi_{\rm s}(\boldsymbol{q})}{\partial q_i}, \tag{A10}$$

$$\Psi_i^{(l)\prime} + \mathcal{H}\Psi_i^{(l)\prime} = -\mathcal{T}_\tau(\eta, k_{\rm L})\xi_{{\rm ini}ia}q_a. \tag{A11}$$

Using the Poisson equation (A6), the solution of Eq. (A10) is given by

$$\Psi_i^{(s)}(\eta, \boldsymbol{q}) = -D(\eta)\partial_q^{-2}\frac{\partial}{\partial q_i}\delta^{(1)}(\eta_0, \boldsymbol{q}), \tag{A12}$$

where the quantity η_0 is the conformal time at the present time. The linear growth factor $D(\eta)$ satisfies

$$D''(\eta) + \mathcal{H}D'(\eta) - 4\pi G a^2\bar{\rho}_{\rm m}D(\eta) = 0. \tag{A13}$$

We adopt the normalization conditions $D(\eta_0) = 1$. The solution of Eq. (A11) is given by

$$\Psi_i^{(l)} = -\beta(\eta, k_{\rm L})\xi_{{\rm ini}ia}q_a, \tag{A14}$$

where we define

$$\beta(\eta, k_{\rm L}) = -\int_0^\eta \frac{{\rm d}\eta'}{a(\eta')}\int_0^{\eta'} a(\eta'')\mathcal{T}_\tau(\eta'', k_{\rm L}){\rm d}\eta''. \tag{A15}$$

Next, we solve the equation for $\boldsymbol{\Psi}$ by considering only the coupling between long- and short-wavelength modes. We start by taking the divergence of Eq. (A5) with respect to $\boldsymbol{q}$:

$$\Psi_{a,a}^{(sl)\prime\prime} + \mathcal{H}\Psi_{a,a}^{(sl)\prime} = -\nabla_x^2\phi_{\rm s} - \Psi_{b,a}^{(s)}\tau_{ab} - \Psi_{b,a}^{(l)}\partial_{x_b}\partial_{x_a}\phi_{\rm s}, \tag{A16}$$

where a comma stands for the derivative with respect to the Lagrangian coordinate. We note that the first term on the right-hand side involves the coupling of short- and long-wavelength modes through the chain rule of spatial difference: $\frac{\partial}{\partial x_i} = (J^{-1})_{ji}\frac{\partial}{\partial q_j}$ with the Jacobian matrix $J_{ij} = \frac{\partial x_i}{\partial q_j} = \delta_{ij} + \Psi_{i,j}$. Then, the second order equation for $\boldsymbol{\Psi}^{(sl)}$ is given by

$$\begin{aligned}\Psi_{a,a}^{(sl)\prime\prime} + \mathcal{H}\Psi_{a,a}^{(sl)\prime} - 4\pi G a^2\bar{\rho}_{\rm m}\Psi_{a,a}^{(sl)} \\ = \mathcal{T}_\tau(\eta, k_{\rm L})D(\eta)\partial_q^{-2}\frac{\partial^2\delta^{(1)}(\eta_0, \boldsymbol{q})}{\partial q_a\partial q_b}\xi_{{\rm ini}ab.}\end{aligned} \tag{A17}$$

The solution of this equation is given by

$$\Psi_{a,a}^{(sl)} = D^{(sl)}(\eta, k_{\rm L})\partial_q^{-2}\frac{\partial^2\delta^{(1)}(\eta_0)}{\partial q_a\partial q_b}\xi_{{\rm ini}ab}(k_{\rm L}), \tag{A18}$$

where the function $D^{sl}(\eta, k_{\rm L})$ satisfies

$$D^{(sl)\prime\prime} + \mathcal{H}D^{(sl)\prime} - 4\pi G a^2\bar{\rho}_{\rm m}D^{(sl)} = D(\eta)\mathcal{T}_\tau(\eta, k_{\rm L}). \tag{A19}$$

From Eqs. (A12), (A14), and (A17), we obtain the Eulerian density field up to the second order:

$$\delta(\boldsymbol{x}) = \delta^{(s)}(\boldsymbol{x}) + \delta^{(sl)}(\boldsymbol{x}), \tag{A20}$$

where we define

$$\begin{aligned}\delta^{(s)}(\boldsymbol{x}) &= -\Psi_{a,a}^{(s)}(\boldsymbol{x}), \\ &= D(\eta)\delta^{(1)}(\eta_0, \boldsymbol{x}),\end{aligned} \tag{A21}$$

$$\begin{aligned}\delta^{(sl)}(\boldsymbol{x}) &= \Psi_{a,ab}^{(s)}(\boldsymbol{x})\Psi_b^{(l)}(\boldsymbol{x}) - \Psi_{a,a}^{(sl)}(\boldsymbol{x}) \\ &\quad + \Psi_{a,a}^{(s)}(\boldsymbol{x})\Psi_{b,b}^{(l)}(\boldsymbol{x}) + \Psi_{a,b}^{(s)}(\boldsymbol{x})\Psi_{b,a}^{(l)}(\boldsymbol{x}),\end{aligned} \tag{A22}$$

$$\begin{aligned}&= \xi_{{\rm ini}ab}(k_{\rm L})\Big[\beta(\eta, k_{\rm L})x_a\partial_b \\ &\quad + \left(-\frac{D^{(sl)}(\eta, k_{\rm L})}{D(\eta)} + \beta(\eta, k_{\rm L})\right)\partial^{-2}\partial_a\partial_b\Big]\delta^{(1)}(\boldsymbol{x}).\end{aligned} \tag{A23}$$

We use the same ansatz in Ref. [85] which assumes that the second term in the square brackets in Eq. (A23) induces the IAs, since this term represents the growth of the density perturbation in a local region by the coupling between the long- and short-wavelength tidal fields while the first term corresponds to the displacement induced by the long-wavelength tidal field, which should have no effect on local physics. We also assume that the alignment from the vector/tensor tidal fields has the same scaling as the second order density induced by the scalar tidal fields. According to this ansatz, the expression of the intrinsic galaxy shape is given by

$$\gamma_{ij} = b_{\rm K}(\eta, k_{\rm L})\xi_{{\rm ini}ij}, \tag{A24}$$

$$b_{\rm K}(\eta, k_{\rm L}) \equiv \frac{7}{4}\left(-\frac{D^{(sl)}(\eta, k_{\rm L})}{D(\eta)} + \beta(\eta, k_{\rm L})\right) b_{\rm K}^{\rm scalar}, \tag{A25}$$

where $b_{\rm K}^{\rm scalar}$ is the scalar linear shape bias. The factor $7/4$ comes from the conversion from the second-order density field to the galaxy intrinsic shape in the scalar mode case [85,86].

APPENDIX B: ONE LOOP CONTRIBUTIONS TO B MODE POWER SPECTRUM

Here we give a brief explanation of what is assumed to compute the one-loop correction to the B-mode auto power spectrum. Recently the perturbation theory of the IAs with the effective theory considerations has been formulated in both Eulerian and Lagrangian ways [105,120]. In this paper we employ the LPT-based calculation of the one-loop power spectrum developed in Ref. [105].

As the one-loop power spectrum involves the linear, quadratic, and cubic fields, we need to introduce up to the cubic shape bias parameters, which in general consist of one linear, three quadratic, and two cubic free parameters to compute the one-loop correction to the shape power spectrum. However, with the comparison of the N-body halo shapes, Ref. [121] showed that the values of the higher order (Eulerian) shape bias parameters are well approximated by the coevolution prediction [122]. In other words, the halo shape field is well described by the Lagrangian tracer of the initial tidal field advected to its final position by the large-scale bulk flow. Hence the following model can be used in lieu of the full model for the one-loop power spectrum:

$$\gamma_{ij}(\mathbf{k}) = \int {\rm d}^3\mathbf{q}\gamma_{ij}^{\rm L}(\mathbf{q})e^{i\mathbf{k}\cdot(\mathbf{q}+\mathbf{\Psi}(\mathbf{q}))}, \tag{B1}$$

with

$$\gamma_{ij}^{\rm L}(\mathbf{q}) = b_{\rm K}^{\rm L}K_{ij}(\mathbf{q})[1+\delta_g^{\rm L}(\mathbf{q})], \tag{B2}$$

where $b_{\rm K}^{\rm L}$ is the Lagrangain linear shape bias and $\delta_g^{\rm L}(\mathbf{q})$ is the Lagrangian galaxy density field. Note that since the galaxy shapes are always observed with galaxies they are naturally density-weighted quantities.

In order to compute the one-loop correction, we can also assume the linear bias description for the galaxy density field since the quadratic bias fields in the density in Eq. (B2) give rise to a reparametrization of the linear shape bias parameter. After all, with these assumptions, the free bias parameters we have to include to the one-loop calculation are the linear shape and density bias parameters: $b_{\rm K}^{\rm L}$ and $b_1^{\rm L}$. The Lagrangian linear shape bias is the same as the Eulerian one, $b_{\rm K}^{\rm scalar} = b_{\rm K}^{\rm L}$, since the tidal field does not induce the volume distortion at first order, while the Lagrangian linear density bias is related to the Eulerian one as $b_1^{\rm E} = b_1^{\rm L} + 1$. Using these relations we can compute the one-loop correction to the shape power spectrum given the values of $b_{\rm K}^{\rm scalar}$ and $b_1^{\rm E}$.

APPENDIX C: FISHER FORECAST FOR THE VORTICITY VECTOR MODE AND PRIMORDIAL GWs

As we are interested in the detectability of the PMFs through observations of the galaxy shape, we have focused on the vector and tensor modes induced by PMFs in the main text. For reference purposes, this appendix provides the Fisher forecast based on the same analysis as done in Sec. V, but we consider other vector and tensor sources: the vorticity vector mode and the primordial GWs.

We define the Fisher matrix for a fixed spectral index $n_V = n_T = 0$ by

$$F(r_{X,{\rm fid}}) = \frac{V}{2(2\pi)^2}\int_{k_{\rm min}}^{k_{\rm max}} k^2{\rm d}k\int_{-1}^{1}{\rm d}\mu \times \sum_{a=EE,BB}\left(\frac{\partial P_a}{\partial r_X}\frac{1}{P_a+\sigma_\gamma^2/n_{\rm gal}}\bigg|_{r_X=r_{X,{\rm fid}}}\right)^2, \tag{C1}$$

where $X = V$ and T for the vorticity vector mode and the primordial GWs, respectively. The size of the expected error on the amplitude of the vector/tensor modes is given by $\sigma(r_{X,{\rm fid}}) = \sqrt{F^{-1}(r_{X,{\rm fid}})}$. We here evaluate the minimum detectable value $r_{X,{\rm min}}$ by solving

$$\sigma(r_{X,{\rm min}}) = r_{X,{\rm min}}. \tag{C2}$$

Table I shows the results for the Euclid spectroscopic survey and SKA HI galaxy survey. We see from this that the E-mode (B-mode) power spectrum can capture smaller r_T (r_V) than the B-mode (E-mode) one. This can happen in surveys where the covariance is dominated by the shot noise as with the Euclid and SKA. For the primordial GW case, ignoring the cosmic variance contribution to the

TABLE I. Minimum detectable value for the spectroscopic survey in Euclid (left values) and SKA (right values). For the spectral index of the vorticity vector mode and primordial GWs, we set $n_V = n_T = 0$.

Euclid/SKA	Vorticity vector $10^{-5} r_V$	Primordial GWs $10^{-5} r_T$
EE	2.95/0.84	4.45/1.45
BB	0.631/0.171	5.35/1.66
EE + BB	0.615/0.167	3.19/1.04

covariance, we can analytically estimate the ratio of the Fisher matrix $F^{(T)}_{EE}/F^{(T)}_{BB}$ by

$$\frac{F^{(T)}_{EE}}{F^{(T)}_{BB}} \approx \frac{\int^1_{-1} d\mu P^{(T)}_{EE}}{\int^1_{-1} d\mu P^{(T)}_{BB}} \approx \frac{\left(\frac{1}{16}\int^1_{-1} d\mu (1+\mu^2)^2\right)^2}{\left(\frac{1}{4}\int^1_{-1} d\mu \mu^2\right)^2} = \frac{83}{63}, \tag{C3}$$

yielding $\sigma_{EE}(r_T) \approx \sqrt{63/83}\sigma_{BB}(r_T) = 0.87\sigma_{BB}(r_T)$. Similarly, in the vorticity vector mode case, we have $\sigma_{EE}(r_V) \approx \sqrt{21}\sigma_{BB}(r_V) = 4.6\sigma_{BB}(r_V)$. These values explain the results in Table I very well. We note that the minimum detectable value given in Table I is larger than the constraints derived in Ref. [87] because our analysis assumes the spectroscopic survey which has generally a smaller number of galaxies than the photometric surveys assumed in Ref. [87].

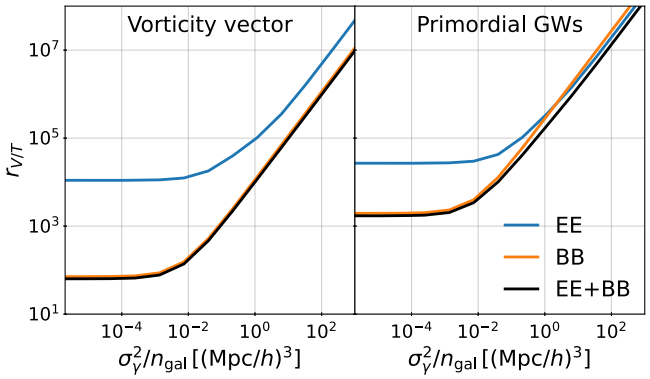

FIG. 7. Same as Fig. 6 but for the vorticity vector mode and primordial GWs.

In Fig. 7, we perform the same analysis as in Fig. 6 but for the cases of the vorticity vector mode and primordial GWs. In analogy with the magnetic case in Fig. 6, as the shot noise decreases, the detectability of $r_{V/T}$ from the E and B modes reaches a plateau because of the scalar-mode contamination in the covariance. In a noisy regime as $10^0(\mathrm{Mpc}/h)^3 \lesssim \sigma^2_\gamma/n_{\rm gal}$, as the above analytic estimate indicates, the E-mode spectrum can capture smaller r_T than the B-mode one.

[1] A. Neronov and I. Vovk, Science **328**, 73 (2010).
[2] F. Tavecchio, G. Ghisellini, G. Bonnoli, and L. Foschini, Mon. Not. R. Astron. Soc. **414**, 3566 (2011).
[3] I. Vovk, A. M. Taylor, D. Semikoz, and A. Neronov, Astrophys. J. Lett. **747**, L14 (2012).
[4] K. Takahashi, M. Mori, K. Ichiki, S. Inoue, and H. Takami, Astrophys. J. Lett. **771**, L42 (2013).
[5] Y.-P. Yang and Z.-G. Dai, Res. Astron. Astrophys. **15**, 2173 (2015).
[6] P. Veres, C. D. Dermer, and K. S. Dhuga, Astrophys. J. **847**, 39 (2017).
[7] D. Grasso and H. R. Rubinstein, Phys. Rep. **348**, 163 (2001).
[8] R. Durrer and A. Neronov, Astron. Astrophys. Rev. **21**, 62 (2013).
[9] K. Subramanian, Rep. Prog. Phys. **79**, 076901 (2016).
[10] M. S. Turner and L. M. Widrow, Phys. Rev. D **37**, 2743 (1988).
[11] B. Ratra, Astrophys. J. Lett. **391**, L1 (1992).
[12] A. D. Dolgov, Phys. Rev. D **48**, 2499 (1993).
[13] K. Bamba and J. Yokoyama, Phys. Rev. D **69**, 043507 (2004).
[14] V. Demozzi, V. Mukhanov, and H. Rubinstein, J. Cosmol. Astropart. Phys. 08 (2009) 025.
[15] A. Kandus, K. E. Kunze, and C. G. Tsagas, Phys. Rep. **505**, 1 (2011).
[16] C. Caprini and L. Sorbo, J. Cosmol. Astropart. Phys. 10 (2014) 056.
[17] G. Domènech, C. Lin, and M. Sasaki, Europhys. Lett. **115**, 19001 (2016).
[18] H. Bazrafshan Moghaddam, E. McDonough, R. Namba, and R. H. Brandenberger, Classical Quantum Gravity **35**, 105015 (2018).
[19] Y. V. Shtanov and M. V. Pavliuk, Ukr. Phys. J. **64**, 1009 (2019).
[20] Y. Shtanov, J. Cosmol. Astropart. Phys. 10 (2019) 008.
[21] A. Talebian, A. Nassiri-Rad, and H. Firouzjahi, Phys. Rev. D **102**, 103508 (2020).
[22] A. Talebian, A. Nassiri-Rad, and H. Firouzjahi, Phys. Rev. D **105**, 023528 (2022).
[23] T. Vachaspati, Phys. Lett. B **265**, 258 (1991).
[24] G. Sigl, A. V. Olinto, and K. Jedamzik, Phys. Rev. D **55**, 4582 (1997).
[25] A. G. Tevzadze, L. Kisslinger, A. Brandenburg, and T. Kahniashvili, Astrophys. J. **759**, 54 (2012).
[26] Y. Zhang, T. Vachaspati, and F. Ferrer, Phys. Rev. D **100**, 083006 (2019).

[27] J. Ellis, M. Fairbairn, M. Lewicki, V. Vaskonen, and A. Wickens, J. Cosmol. Astropart. Phys. 09 (2019) 019.
[28] Y. Di, J. Wang, R. Zhou, L. Bian, R.-G. Cai, and J. Liu, Phys. Rev. Lett. **126**, 251102 (2021).
[29] J. Yang and L. Bian, Phys. Rev. D **106**, 023510 (2022).
[30] E. R. Harrison, Mon. Not. R. Astron. Soc. **147**, 279 (1970).
[31] K. Takahashi, K. Ichiki, H. Ohno, and H. Hanayama, Phys. Rev. Lett. **95**, 121301 (2005).
[32] E. Fenu, C. Pitrou, and R. Maartens, Mon. Not. R. Astron. Soc. **414**, 2354 (2011).
[33] S. Saga, K. Ichiki, K. Takahashi, and N. Sugiyama, Phys. Rev. D **91**, 123510 (2015).
[34] C. Fidler, G. Pettinari, and C. Pitrou, Phys. Rev. D **93**, 103536 (2016).
[35] C. Caprini and R. Durrer, Phys. Rev. D **65**, 023517 (2001).
[36] D. G. Yamazaki and M. Kusakabe, Phys. Rev. D **86**, 123006 (2012).
[37] M. Kawasaki and M. Kusakabe, Phys. Rev. D **86**, 063003 (2012).
[38] Y. Luo, T. Kajino, M. Kusakabe, and G. J. Mathews, Astrophys. J. **872**, 172 (2019).
[39] M. Kusakabe, A. Kedia, G. J. Mathews, and N. Sasankan, Phys. Rev. D **104**, 123534 (2021).
[40] Y. Lu and M. Kusakabe, Astrophys. J. Lett. **926**, L4 (2022).
[41] R. Durrer, P. G. Ferreira, and T. Kahniashvili, Phys. Rev. D **61**, 043001 (2000).
[42] A. Lewis, Phys. Rev. D **70**, 043011 (2004).
[43] M. Giovannini, Phys. Rev. D **70**, 123507 (2004).
[44] F. Finelli, F. Paci, and D. Paoletti, Phys. Rev. D **78**, 023510 (2008).
[45] D. Paoletti, F. Finelli, and F. Paci, Mon. Not. R. Astron. Soc. **396**, 523 (2009).
[46] J. R. Shaw and A. Lewis, Phys. Rev. D **81**, 043517 (2010).
[47] C. Bonvin, C. Caprini, and R. Durrer, Phys. Rev. D **88**, 083515 (2013).
[48] S. Saga, A. Ota, H. Tashiro, and S. Yokoyama, Mon. Not. R. Astron. Soc. **490**, 4419 (2019).
[49] K. Jedamzik and A. Saveliev, Phys. Rev. Lett. **123**, 021301 (2019).
[50] T. Minoda, K. Ichiki, and H. Tashiro, J. Cosmol. Astropart. Phys. 03 (2021) 093.
[51] S. Mandal, N. Sehgal, and T. Namikawa, Phys. Rev. D **105**, 063537 (2022).
[52] K. Jedamzik, V. Katalinić, and A. V. Olinto, Phys. Rev. Lett. **85**, 700 (2000).
[53] K. E. Kunze and E. Komatsu, J. Cosmol. Astropart. Phys. 01 (2014) 009.
[54] S. Saga, H. Tashiro, and S. Yokoyama, Mon. Not. R. Astron. Soc. **474**, L52 (2018).
[55] D. Ryu, D. R. G. Schleicher, R. A. Treumann, C. G. Tsagas, and L. M. Widrow, Space Sci. Rev. **166**, 1 (2012).
[56] J. R. Shaw and A. Lewis, Phys. Rev. D **86**, 043510 (2012).
[57] C. Fedeli and L. Moscardini, J. Cosmol. Astropart. Phys. 11 (2012) 055.
[58] S. Camera, C. Fedeli, and L. Moscardini, J. Cosmol. Astropart. Phys. 03 (2014) 027.
[59] A. Heavens, A. Refregier, and C. Heymans, Mon. Not. R. Astron. Soc. **319**, 649 (2000).
[60] R. A. C. Croft and C. A. Metzler, Astrophys. J. **545**, 561 (2000).
[61] P. Catelan and C. Porciani, Mon. Not. R. Astron. Soc. **323**, 713 (2001).
[62] R. G. Crittenden, P. Natarajan, U.-L. Pen, and T. Theuns, Astrophys. J. **559**, 552 (2001).
[63] C. M. Hirata and U. Seljak, Phys. Rev. D **70**, 063526 (2004).
[64] R. Mandelbaum, C. M. Hirata, M. Ishak, U. Seljak, and J. Brinkmann, Mon. Not. R. Astron. Soc. **367**, 611 (2006).
[65] C. M. Hirata, R. Mandelbaum, M. Ishak, U. Seljak, R. Nichol, K. A. Pimbblet, N. P. Ross, and D. Wake, Mon. Not. R. Astron. Soc. **381**, 1197 (2007).
[66] T. Okumura, Y. P. Jing, and C. Li, Astrophys. J. **694**, 214 (2009).
[67] M. A. Troxel and M. Ishak, Phys. Rep. **558**, 1 (2015).
[68] F. Schmidt and D. Jeong, Phys. Rev. D **86**, 083513 (2012).
[69] N. E. Chisari and C. Dvorkin, J. Cosmol. Astropart. Phys. 12 (2013) 029.
[70] T. Okumura, A. Taruya, and T. Nishimichi, Phys. Rev. D **100**, 103507 (2019).
[71] T. Okumura and A. Taruya, Mon. Not. R. Astron. Soc. **493**, L124 (2020).
[72] A. Taruya and T. Okumura, Astrophys. J. Lett. **891**, L42 (2020).
[73] M. Shiraishi, A. Taruya, T. Okumura, and K. Akitsu, Mon. Not. R. Astron. Soc. **503**, L6 (2021).
[74] K. Akitsu, T. Kurita, T. Nishimichi, M. Takada, and S. Tanaka, Phys. Rev. D **103**, 083508 (2021).
[75] K. Kogai, K. Akitsu, F. Schmidt, and Y. Urakawa, J. Cosmol. Astropart. Phys. 03 (2021) 060.
[76] T. Okumura and A. Taruya, Phys. Rev. D **106**, 043523 (2022).
[77] Y.-T. Chuang, T. Okumura, and M. Shirasaki, Mon. Not. R. Astron. Soc. **515**, 4464 (2022).
[78] S. Saga, T. Okumura, A. Taruya, and T. Inoue, Mon. Not. R. Astron. Soc. **518**, 4976 (2023).
[79] M. Shiraishi, T. Okumura, and K. Akitsu, J. Cosmol. Astropart. Phys. 08 (2023) 013.
[80] T. Kurita and M. Takada, Phys. Rev. D **108**, 083533 (2023).
[81] T. Okumura and A. Taruya, Astrophys. J. Lett. **945**, L30 (2023).
[82] K. W. Masui and U.-L. Pen, Phys. Rev. Lett. **105**, 161302 (2010).
[83] D. Jeong and M. Kamionkowski, Phys. Rev. Lett. **108**, 251301 (2012).
[84] L. Dai, D. Jeong, and M. Kamionkowski, Phys. Rev. D **88**, 043507 (2013).
[85] F. Schmidt, E. Pajer, and M. Zaldarriaga, Phys. Rev. D **89**, 083507 (2014).
[86] K. Akitsu, Y. Li, and T. Okumura, Phys. Rev. D **107**, 063531 (2023).
[87] O. H. E. Philcox, M. J. König, S. Alexander, and D. N. Spergel, arXiv:2309.08653.
[88] A. Lewis, Phys. Rev. D **70**, 043518 (2004).
[89] A. Mack, T. Kahniashvili, and A. Kosowsky, Phys. Rev. D **65**, 123004 (2002).
[90] M. Giovannini and K. E. Kunze, Phys. Rev. D **77**, 063003 (2008).

[91] Planck Collaboration, Astron. Astrophys. **594**, A19 (2016).
[92] K. Subramanian and J. D. Barrow, Phys. Rev. D **58**, 083502 (1998).
[93] A. Lewis, A. Challinor, and A. Lasenby, Astrophys. J. **538**, 473 (2000).
[94] S. Saga, H. Tashiro, and S. Yokoyama, Phys. Rev. D **98**, 083518 (2018).
[95] K. Ichiki, K. Takahashi, and N. Sugiyama, Phys. Rev. D **85**, 043009 (2012).
[96] S. Saga, M. Shiraishi, and K. Ichiki, J. Cosmol. Astropart. Phys. 10 (2014) 004.
[97] W. R. Coulton, K. Akitsu, and M. Takada, Phys. Rev. D **108**, 123528 (2023).
[98] E. Pajer, F. Schmidt, and M. Zaldarriaga, Phys. Rev. D **88**, 083502 (2013).
[99] L. Dai, E. Pajer, and F. Schmidt, J. Cosmol. Astropart. Phys. 11 (2015) 043.
[100] S. Dodelson, E. Rozo, and A. Stebbins, Phys. Rev. Lett. **91**, 021301 (2003).
[101] C. Li and A. Cooray, Phys. Rev. D **74**, 023521 (2006).
[102] D. Yamauchi, T. Namikawa, and A. Taruya, J. Cosmol. Astropart. Phys. 10 (2012) 030.
[103] D. Yamauchi, T. Namikawa, and A. Taruya, J. Cosmol. Astropart. Phys. 08 (2013) 051.
[104] S. Saga, D. Yamauchi, and K. Ichiki, Phys. Rev. D **92**, 063533 (2015).
[105] S.-F. Chen and N. Kokron, J. Cosmol. Astropart. Phys. 01 (2024) 027.
[106] Planck Collaboration, Astron. Astrophys. **641**, A6 (2020).
[107] K. Akitsu, Y. Li, and T. Okumura, J. Cosmol. Astropart. Phys. 04 (2021) 041.
[108] P. Bull, Astrophys. J. **817**, 26 (2016).
[109] C. M. Hirata and U. Seljak, Phys. Rev. D **68**, 083002 (2003).
[110] F. Schmidt, E. Rozo, S. Dodelson, L. Hui, and E. Sheldon, Astrophys. J. **702**, 593 (2009).
[111] D. Paoletti and F. Finelli, Phys. Rev. D **83**, 123533 (2011).
[112] R. Laureijs *et al.*, arXiv:1110.3193.
[113] D. J. Bacon *et al.* (Square Kilometre Array Cosmology Science Working Group), Publ. Astron. Soc. Aust. **37**, e007 (2020).
[114] R. Mandelbaum *et al.*, Mon. Not. R. Astron. Soc. **410**, 844 (2011).
[115] M. Tonegawa, T. Okumura, T. Totani, G. Dalton, K. Glazebrook, and K. Yabe, Publ. Astron. Soc. Jpn. **70**, 41 (2018).
[116] M. Tonegawa and T. Okumura, Astrophys. J. Lett. **924**, L3 (2022).
[117] J. Shi, K. Osato, T. Kurita, and M. Takada, Astrophys. J. **917**, 109 (2021).
[118] Euclid Collaboration, Astron. Astrophys. **642**, A191 (2020).
[119] P. Bull, S. Camera, A. Raccanelli, C. Blake, P. Ferreira, M. Santos, and D. J. Schwarz, Proc. Sci. AASKA14 (**2015**) 024 [arXiv:1501.04088].
[120] Z. Vlah, N. E. Chisari, and F. Schmidt, J. Cosmol. Astropart. Phys. 01 (2020) 025.
[121] K. Akitsu, Y. Li, and T. Okumura, J. Cosmol. Astropart. Phys. 08 (2023) 068.
[122] D. M. Schmitz, C. M. Hirata, J. Blazek, and E. Krause, J. Cosmol. Astropart. Phys. 07 (2018) 030.